Journal of
Synchrotron Radiation

ISSN 0909-0495

Received 15 June 2004
Accepted 6 December 2004

X-ray vision of fuel sprays

Jin Wang

Experimental Facilities Division, Argonne National Laboratory, Argonne, IL 60439, USA.
E-mail: wangj@aps.anl.gov

With brilliant synchrotron X-ray sources, microsecond time-resolved synchrotron X-ray radiography and tomography have been used to elucidate the detailed three-dimensional structure and dynamics of high-pressure high-speed fuel sprays in the near-nozzle region. The measurement allows quantitative determination of the fuel distribution in the optically impenetrable region owing to the multiple scattering of visible light by small atomized fuel droplets surrounding the jet. X-radiographs of the jet-induced shock waves prove that the fuel jets become supersonic under appropriate injection conditions and that the quantitative analysis of the thermodynamic properties of the shock waves can also be derived from the most direct measurement. In other situations where extremely axial-asymmetric sprays are encountered, mass deconvolution and cross-sectional fuel distribution models can be computed based on the monochromatic and time-resolved X-radiographic images collected from various rotational orientations of the sprays. Such quantitative analysis reveals the never-before-reported characteristics and most detailed near-nozzle mass distribution of highly transient fuel sprays.

Keywords: fuel sprays; direct injection; radiography; tomography; reconstruction; shock wave; time-resolved imaging.

1. Introduction

High-pressure high-speed sprays are an essential technology in many industrial and consumer applications, including fuel injection systems, ink-jet printers, liquid-jet cutting tools and liquid-jet cleaning systems (O'Keefe *et al.*, 1967; Herman, 1988; Tikhomirov *et al.*, 1992; Summers, 1995; Kuo, 1996). Frequently, the liquids are optically dense or the liquid droplets generated by the sprays scatter light so strongly that the detailed structure of the sprays cannot be resolved by conventional optical means (Field & Lesser, 1977). This is especially true in the region near the injection nozzle, which is often the region of greatest interest in understanding the structure of the jet. Other challenges arise from the transient nature of features of the jet sprays, frequently requiring images on microsecond time scales. The lack of quantitative time-resolved analyses on the structure and dynamics of sprays limits the accuracy of spray modeling and creates obstacles to improving spray technology. In particular, liquid fuel sprays and their atomization and combustion processes have numerous technological applications including energy sources for propulsion and transportation systems including internal combustion engines (ICEs). The importance of detailed gasoline and diesel fuel-spray analyses is well recognized as vital information with which to increase the combustion efficiency and reduce the emission of pollutants of ICEs. In these cases, improvements of even a few percent would have enormously important and beneficial economic and social consequences. In the application of compression-ignition direct-injection (CIDI) for diesel sprays, higher injection pressures (>150 MPa) and smaller orifice diameters (<150 μm) for small-bore diesel engines have brought even greater impetus to the understanding of fuel-spray behavior. On the other hand, with the increased global interest in gasoline direct injection (GDI), automotive industries worldwide are taking the initiative to commercially implement this technology, which is considered a major improvement towards cleaner automobile engines as it may offer 15–35% improvement in fuel efficiency (Spearot, 2001). Currently, this technology, however, faces potential problems in controlling particulate matter and nitrides-of-oxygen emissions and fails to meet US government regulatory standards. The environmental concern is one of the main reasons explaining why the technology is yet to be implemented in commercial automobiles in the US (Council, 2001).

In direct-injection (DI) engines, since fuel is directly injected into the cylinder the spray characteristics and mixing process play an important role in the combustion procedure. Thus, knowledge of fuel-spray behavior in combustion systems is recognized as a key to increasing combustion efficiency and reducing pollutant emissions (Zhao *et al.*, 1999). Thorough understanding of the fuel density distribution in the near-nozzle region is particularly important with regard to DI sprays. An understanding of the liquid breakup mechanism in

the region close to the nozzle is also vital to realistic computational modeling and has significant bearing on the design of nozzle geometry. These interests have spurred considerable activity in the development of optical techniques for measurements. Despite significant advances in spray diagnostics over the last 20 years, the region close to the nozzle has not satisfactorily yielded to experiments designed to acquire quantitative information (Yule & Watkins, 1990; Adrian, 1991; Chigier, 1991; Hentschel & Schindler, 1996; Fujikawa *et al.*, 1999; Beeck & Hentschel, 2000; Cao *et al.*, 2000; Zhang *et al.*, 2000; Lee *et al.*, 2001; Sick & Stojkovic, 2001; Ullom & Sojka, 2001). Multiple scattering from the large number of droplets prevents the penetration of light in this near-nozzle region and thus limits quantitative evaluation with these techniques. Fuel spray characterization has been difficult also because it requires microsecond time resolution of submillimeter-scale structures in a complex mixture of liquid and gas. Mechanical techniques, such as patternators, are capable of probing the near-nozzle region but perturb the spray and have limited spatial and temporal resolution (Hoffman *et al.*, 1997; Parrish & Farrell, 1997). While many other researchers are looking into the possibility of using ultrahigh-power lasers to penetrate this region, this paper reviews the development of a new nonintrusive and highly time-resolved (1 μs or better) technique to characterize the dense part of the fuel spray using X-radiography, which has proven to yield unique and more quantitative information than any conventional nonoptical or optical technique (Powell *et al.*, 2000; MacPhee *et al.*, 2002; Cai *et al.*, 2003).

X-rays are highly penetrative in low-atomic-number materials of extremely dense droplets owing to their intrinsically low cross section when interacting with matter, and multiple scattering is typically a negligible component in such systems. This makes X-rays a useful tool for spray studies designed to overcome the limitation of visible light. Previously, researchers (Char *et al.*, 1990; Woodward *et al.*, 1995) used X-ray tube sources to perform radiographic studies of the liquid core structure of coaxial jets of high-Z materials on a relatively large scale (nozzle diameter 5 mm). However, when an energy-dispersive X-ray beam is used as the radiographic light source, the transmission of the X-ray beams (I/I_0, where I_0 and I are the incident and transmitted intensity, respectively) is described by

$$I/I_0 = \int \rho(\lambda) \exp\left[-\mu_M(\lambda) M\right] \mathrm{d}\lambda \,/\, \int \rho(\lambda)\, \mathrm{d}\lambda, \qquad (1)$$

where $\rho(\lambda)$ is a wavelength (λ) dependent function that describes the incident beam spectrum and the detector response, while $\mu_M(\lambda)$ is the mass absorption coefficient and M is the total sample mass in the beam. Because of the λ dependence, a precise and quantitative analysis of the absorption is extremely difficult if not impossible. Therefore, a quantitative study of sprays must utilize a monochromatic X-ray beam. For single-wavelength X-rays transmitting through an attenuating material, the analysis of the radiographic image of the attenuating material is straightforward and follows the form

$$I/I_0 = \exp(-\mu_M M). \qquad (2)$$

Since μ_M can be measured accurately for the absorbing medium at a single wavelength, the amount of fuel in the beam path can be easily deduced from the transmission, I/I_0. With the advent of synchrotron X-ray sources, extremely brilliant monochromatic X-ray beams are now available. These sources have paved the way for fast experiments of this type using monochromatic beams and achieving a time resolution of 1 μs or better. For example, at the Advanced Photon Source (APS) bending-magnet beamlines, the high-energy storage ring produces brilliant wide-band X-ray beams of the order of 10^{17} photons s^{-1}. Even with high monochromaticity (*e.g.* 1.5×10^{-4} bandwidth), one can obtain 10^{12} photons s^{-1} focused to a 0.6 mm × 0.3 mm beam spot (Lang *et al.*, 1999).

In this article, we summarize the first several attempts, by using synchrotron X-radiography and novel fast X-ray detectors, to study fuel sprays from high-pressure fuel injectors. For the first time, time-resolved X-radiography clearly captures propagation of the spray-induced shock waves in a gaseous medium. It also allows quantitative analysis of the thermodynamic properties of the shock waves, which has been impossible with optical imaging methods. In a separate experiment, microsecond time-resolved synchrotron X-ray radiography and tomography have also been used to elucidate the detailed three-dimensional structure and dynamics of high-pressure GDI sprays. The combination of novel fast-framing pixel array detectors and model-dependent analyses allowed the tomographic reconstruction of the time-dependent spray that typically last for only about 1 ms. The measurements revealed that hollow-cone gasoline sprays have striking features in the critical and highly transient near-nozzle region, including complex traveling density waves and unexpected axially asymmetric flows.

2. Experiments

2.1. X-radiography and optical imaging setup

The time-resolved radiograph experiments on the fuel sprays were normally performed using two methods: (i) by scanning with a small X-ray beam and a point detector, and (ii) by the use of a beam of extended size with a fast area detector. In the first method, the radiographic images of the sprays were collected by a focused and monochromatic synchrotron X-ray beam from the bending-magnet beamline 1-BM at the APS, in conjunction with a fast avalanche photodiode (APD) point detector (Powell *et al.*, 2000). The data were collected by positioning the transient fuel spray between the X-ray beam and an APD and by recording the time-resolved response of the detector on a transient digitizing oscilloscope. To improve the signal-to-noise ratio, each curve is the average of 50 to 100 injection cycles. Repeated experiments demonstrated that the data were perfectly reproducible. Each data point spans a time interval of 3.68 μs, which is the fundamental period of the APS synchrotron storage ring. The data collection was accomplished by successively measuring the absorption for points along the axis of the spray by directing a fine X-ray beam

perpendicular to the spray axis. The X-ray beam was tuned to a photon energy of 6.0 keV to maximize the X-ray absorption of the fuel additive, cerium, above its *L*-resonance edges near 5.7 keV (see §2.2). The focused beam was then further defined by a pair of X-Y slits to a beam size of 200 to 500 μm (horizontal, H) × 50 μm (vertical, V), full width at half-maximum (FWHM). The APD has a fast response of ∼5 ns, which is sufficient to capture transient spray events, which occurred between 300 and 500 μs after the spray was initiated. The point-detection measurements established that the spray had interesting dynamics and repeatable internal structure. However, point-by-point detection is an impractical means to record the details of the spray over a large area and time duration for phenomena such as spatial and temporal propagation of shock waves or the spatially extended GDI sprays. The second method involved imaging of the spray process with a pixel array detector (PAD) (Barna *et al.*, 1997; Rossi *et al.*, 1999) and with a spatially extended wide-bandpass synchrotron X-ray beam at the D-1 beamline of the Cornell High Energy Synchrotron Source (CHESS) (MacPhee *et al.*, 2002; Cai *et al.*, 2003). Because the X-ray beam size in the experiment was 13.5 mm (H) × 2.5 mm (V), the imaged area was built up by shifting the position of the injector relative to the beam and the detector and repeating the injection cycle. The exposure time per frame was set to 5.13 μs (twice the CHESS synchrotron period of 2.56 μs) with subsequent images taken after an additional 2.56 to 15.4 μs delay. Each position shown is the average of images from 10 to 40 fuel injection cycles. The area detection method not only provided a much more efficient data-collection process but also was a practical technique with which to visualize the shock waves induced by the spray and the large sprays from a GDI injector. Both methods used a similar experimental setup as shown schematically in Fig. 1. In the data-collection apparatus, the injection system, the detectors and the beam shutter are synchronized with the storage ring with a timing jitter estimated to be less than 1 μs.

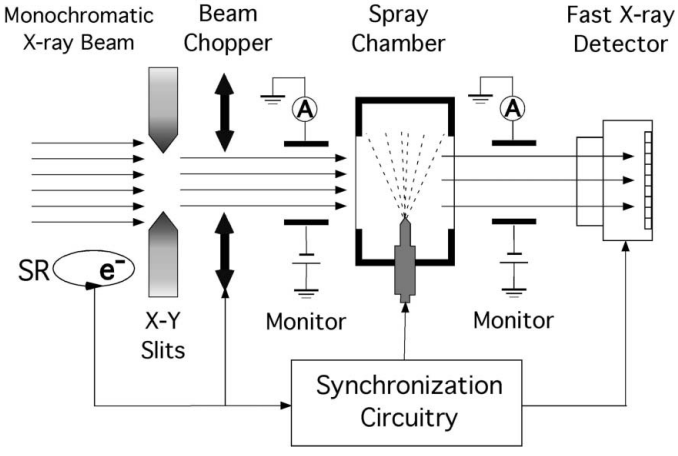

Figure 1
Schematic of the experimental setup. Components, such as the injection system, the detector and the X-ray shutter are synchronized to the storage ring (SR) to ensure minimum timing jitter. In the scanning model, the detector is an APD while in the imaging mode it is a PAD as described in the text. The use of the X-ray shutter is to limit radiation damage to the detector.

Optical Schlieren images (Hecht, 1998) of the shock waves generated by fuel sprays in SF_6 gas were collected prior to the X-ray measurements under similar injection conditions. To visualize the density change in the shock front in the gas medium, flashing white light was collimated by an aperture and a collimating lens before illuminating the fuel sprays. The images were collected at the Schlieren plane. The exposure time was controlled by a gated image intensifier to a duration of about 0.1 μs.

2.2. High-pressure diesel injection system

We used a high-pressure common-rail diesel injection system, typical of that in a passenger car with a specially fabricated single-orifice nozzle. The orifice was specified to be 178 μm in diameter, and the injection pressure can be set at between 20 and 135 MPa. Injection was performed into a spray chamber filled with inert gas at atmospheric pressure and at room temperature (typically 298–303 K). The spray chamber was intended to hold the injector, contain the spray plume, and allow the inert gas to scavenge the fuel vapors. It has two 50 mm × 25 mm windows made of polymer thin films providing line-of-sight access for the X-rays. A gentle flow of inert sulfur hexafluoride (SF_6) gas, with symmetric inlets both above and below the injector, was maintained to scavenge the fuel spray; SF_6, which is a heavy gas (molecular weight of 146), was used to simulate the relatively dense ambient gas environment in a diesel engine during the adiabatic compression part of the engine cycle when the diesel fuel is normally injected. By using SF_6 it was possible to simulate the dense gas environment of the chamber without resorting to high-pressure X-ray windows. Note that the sonic speed in SF_6 at room temperature (303 K) has been measured to be 136 m s^{-1} (Hurly *et al.*, 2000), considerably less than the 330 m s^{-1} speed of sound in air at the same temperature. However, fuel sprays with much higher speeds can be generated at the higher injection pressures often used in diesel engines.

The fuel used in this study was a blend of No. 2 diesel (Amoco) and a cerium (Ce) containing compound (DPX9, Rhodia Terres Rares, 4.2% by weight in the blend). The Ce additive was included to increase the X-ray absorption of the fuel jet and accounted for ∼50% of the total X-ray absorption at the selected beam energy (Henke *et al.*, 1993).

2.3. Injection system for GDI sprays

A GDI injection system with an outwardly opening injector was employed to produce a hollow-cone type of sprays. Injection was performed into a spray chamber filled with nitrogen gas at atmospheric pressure and room temperature. The injection test conditions are summarized in Table 1. The spray chamber is designed like that used in the diesel-spray experiment but with much larger X-ray transparent windows that provide line-of-sight access for the X-rays for the full hollow-cone spray with a large cone-angle. The fuel used in this study was a blend of calibration-type gasoline fuel

Table 1
Summarized GDI test conditions.

Parameters	Quantity and properties
Injection system	GDI, with outwardly opening pintle
Orifice type	Annular
Orifice diameter	1.9 mm
Fill gas	N_2, 0.1 MPa, 298–303 K
Fuel	Viscor calibration fluid with Ce-containing additive
Specific gravity	0.8405 g ml^{-1}
Spray duration	1 ms (nominal)
Spray cone angle	65° (full, 0.1 MPa chamber pressure, nominal)
Region of interest	25 mm from the nozzle

(Viscor) and the Ce-containing additive with a final Ce concentration of 4.2% by weight. Again, the monochromatic X-ray beam tuned to 6.0 keV was used to maximize absorption by the fuel spray.

3. Results

3.1. Shock waves generated by supersonic diesel sprays

For single-wavelength X-rays, the analysis of the transmission of the attenuating material (the fuel) gives an exact measure of the mass in the X-ray beam as described in (2). With the point-by-point method, the time-resolved fuel-mass data measured on the spray axis at 1, 5, 12 and 22 mm from the nozzle are shown in Fig. 2(*a*). The fuel-injection pressure was 50 MPa, and the injection duration was about 800 µs. The four curves are each shown as displaced vertically by 1 µg for clarity. For the data collected at 1 mm, the spray intersected the X-ray beam at $t = 0.17$ ms, evidenced by an abrupt increase of the fuel mass in the X-ray beam from 0 to nearly 5 µg (inside the X-ray beam), indicating a distinct boundary between ambient gas and fuel spray. The sharpness of the interface facilitates the calculation of the apparent speed of the leading edge of the spray, as shown in Fig. 2(*b*). Immediately following the leading edge is a highly concentrated fuel region represented by an extremely sharp peak caused by accumulation of droplets as they impact on the ambient gas at the leading edge. Because the spray is composed of an aerosol of streams and droplets, the liquid at the leading edge of the spray can move at rates quite different than the average body of the spray. Without the resistance or impact to the ambient gas, the spray body can move much faster than the leading edge and with speeds close to that for the trailing edge. While the injection pressure remained stable ($\lesssim 5\%$) during the injection, the fuel mass in the spray body appeared to be fluctuating with rather large amplitudes as a result of the traveling shocks generated by the impact. A shock generated by the impact of the fuel spray on the ambient gas travels within the spray body as a compressed gaseous pocket resulting in a low fuel density region. The result of a rigorous fluid dynamics simulation on this phenomenon is to be published. At a time of 1 ms, a well defined spray trailing edge was also observed indicating that the injection event had finished. The trailing edge of the spray is interesting in that it clearly illustrates the dynamics of the injection process because it moves at an instantaneous speed much greater than the leading edge in the region close to the nozzle, as shown in Fig. 2(*b*). It is quite striking that the trailing-edge speed can be greater than 600 m s^{-1} as the spray exits the nozzle, well above the sonic speed in SF_6 of 136 m s^{-1}. Thereafter, the trailing edge slows to 180 m s^{-1} at 20 mm from the nozzle, roughly equal to the leading-edge speed.

The fluctuations indicate that the axial mass distribution is not uniform throughout the spray body. The first sharp peak in the mass profile is almost certainly caused by mass accumulation as the droplets impact on the chamber gas. The fluctuation, we speculate, is the result of gas entrainment near the nozzle exit. Fortunately, these fluctuations allowed us to perform a correlation calculation for evaluating the internal speed of the spray body as follows. Consider the correlation function, $g(x, \Delta x, t)$, defined by

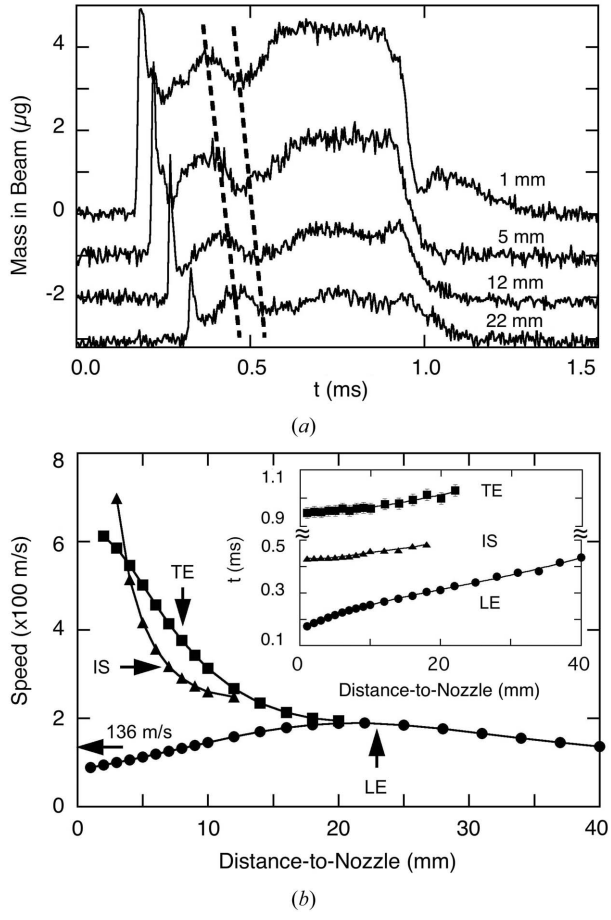

Figure 2
Dynamics of the high-pressure fuel sprays measured with the point-by-point scanning method: (*a*) time evolution of the integrated fuel mass in the X-ray beam on the spray axis at 1, 5, 12 and 22 mm from the nozzle and (*b*) the calculated spray speeds. Each datum point spans a time interval of 3.68 µs. The speed values for the leading edge (LE) and trailing edge (TE) were calculated by the derivative of their penetration curves shown as the inset in (*b*). By tracking the distinctive features, such as the spray internal segment (IS) between the two marker lines in (*a*), the speed of the segment was evaluated with the correlation method illustrated in equation (3).

$$g(x, \Delta x, t) = \int M(x, \tau)\, M(x + \Delta x, \tau + t)\, \mathrm{d}\tau, \qquad (3)$$

where x is the coordinate along the spray axis and Δx is a small displacement at which another time-resolved mass profile was recorded. For practical purposes, Δx can be 1 mm. When the correlation function is calculated with a small fraction of mass profile data, such as those indicated inside the two dashed lines shown in Fig. 2(*a*), one obtains a peak value in the correlation function (equation 3) at $t = \Delta t$. Therefore, the speed of such a fraction of the spray at the location x can be simply estimated by $v(x) = \Delta x/\Delta t$. The speeds that are calculated in this way (Fig. 2*b*) lie between the speeds for the leading and trailing edges but are much closer to that for the trailing edge. Therefore, we conclude that the speed of the major part of the spray travels in the injection chamber with a speed much higher than the speed of sound in the SF_6 gas. In addition, it should be pointed out that the calculation also shows that a small part of the spray has a speed rather similar to that for the leading edge and travels below the speed of sound. Although the point-detector measurements described so far suggested that the fuel spray should generate shock waves, the point-by-point method lacked the spatial resolution and coverage to directly image the shock waves.

To confirm the supersonic nature of the sprays, the shock waves were visualized in the same spray system by optical Schlieren imaging of visible light when the injection pressure reaches 80 MPa, as shown in Fig. 3(*a*). A reflecting wall was also introduced into the testing chamber. The shock front was reflected off this wall and impinges back onto the spray (Fig. 3*b*). The influence of the reflected shock front on the appearance of the spray could not be determined with statistical significance at this time. However, the possibility of enhancing atomization of the liquid fuel near the nozzle by the reflected shock front is of great interest and is currently being investigated. The bright circle in the images indicates the size of the image intensifier, measured at 25 mm in diameter. The imaging magnification in Fig. 3(*b*) was set slightly higher than that in Fig. 3(*a*) to emphasize the region where the reflection of the shock front occurred. The portion of the spray visualized here is the optically dense, low-mass cloud of droplets surrounding the thin main fuel jet that can only be imaged by X-rays.

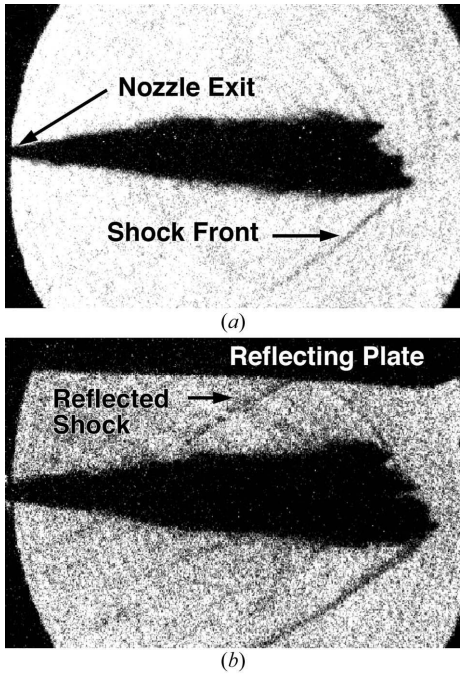

Figure 3
Optical Schlieren images of (*a*) the shock waves generated by fuel sprays in SF_6 gas collected with the injection pressure set at 80 MPa, and (*b*) the effect of a reflecting wall on the shock front. The spray propagates from left to right along the axis of the injector in the imaging field.

As expected, the optical images yielded only the cone-angle of the shock wave; no other quantitative information can be obtained. The direct imaging and the quantitative analysis of the shock waves have become possible with highly brilliant synchrotron X-ray sources and the advent of the PAD. Fig. 4 shows a series of X-radiographs of the fuel spray for times ranging from 38 to 192 µs after the beginning of the injection process. The imaged area shown in the largest panel is 61.7 mm (H) × 17.5 mm (V) with data corrected for the divergence of the X-ray beam. Because the X-ray beam size in the experiment was 13.5 mm (H) × 2.5 mm (V), the imaged area was built up by shifting the position of the injector relative to the beam and the PAD and repeating the injection cycle. Boundaries between these areas can be seen upon close inspection. The exposure time per frame was set to 5.13 µs (twice the CHESS synchrotron period) with subsequent images taken after an additional 2.56 µs delay. Each position shown is the average of images from 20 fuel-injection cycles. The detector was not positioned over all possible areas of the image, so specific images show missing areas. In this measurement, the fuel injection pressure was set to 135 MPa, resulting in maximum leading-edge speeds of 345 m s^{-1}. The leading-edge speed exceeds the sonic speed upon emergence. The shock wavefront, or the so-called Mach cone, is clearly

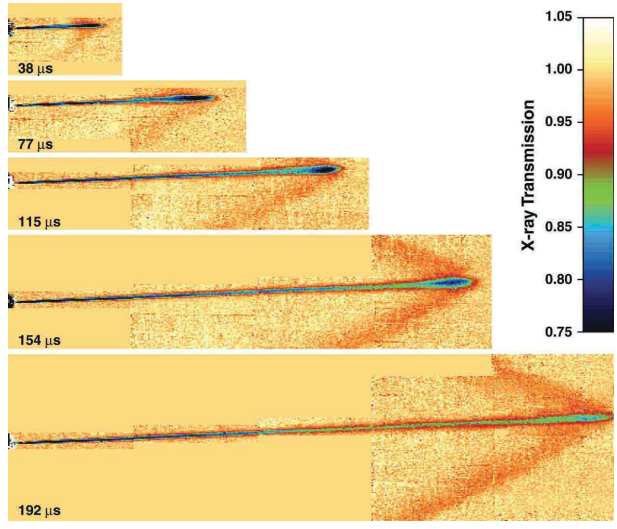

Figure 4
Time-resolved radiographic images of fuel sprays and the shock waves generated by the sprays for time instances of 38, 77, 115, 154 and 192 µs after the start of the injection (selected from the total of 168 frames taken in the radiographic image sequence).

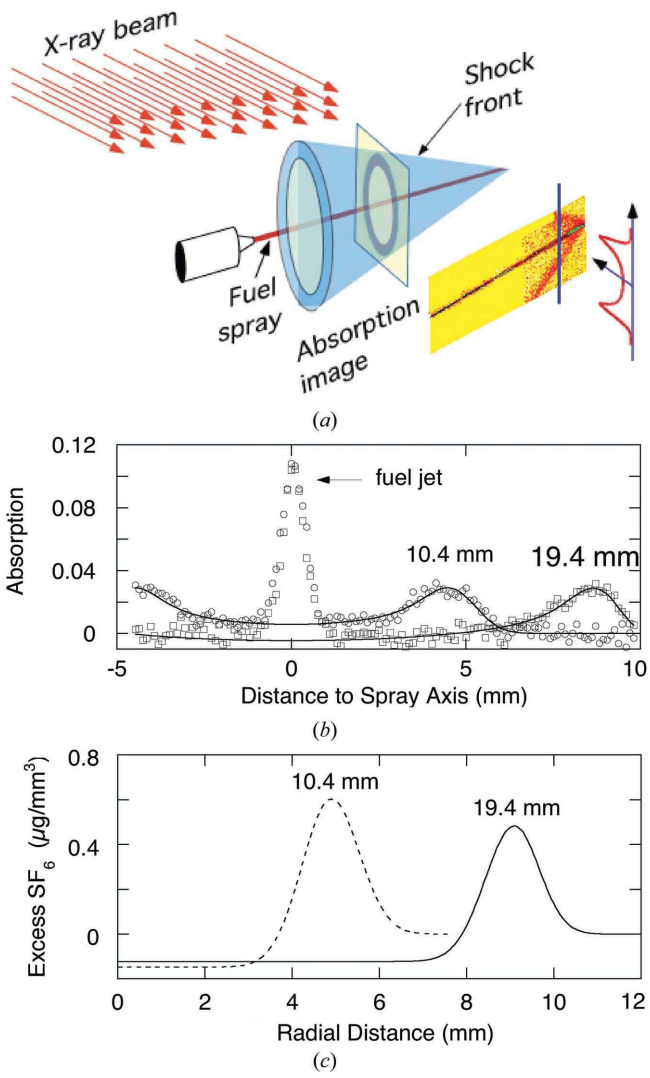

Figure 5
Quantitative analysis of the radiographic images of the Mach cone: (*a*) schematic of the data-collection method, (*b*) deconvolution of the absorption data by the line-of-sight calculation, and (*c*) best fitting models of density distribution of excess ambient gas near the Mach cone.

observed as emanating from the leading edge of the fuel jet soon after emergence with an X-ray absorption of up to 3% in the shock front. The false-color levels of the images have been set to accentuate small differences in the X-ray intensity arising from the slightly increased (~15%) X-ray absorption in the compressed SF_6 gas. The Mach cone angles were also measured at each instance, and the values agreed well with the leading-edge speed determined by the analysis outlined by equation (3).

The quantitative nature of the X-radiograph technique allows us not only to observe the qualitative dynamic evolution of the shock waves but also to derive thermodynamic parameters of interest such as the mass density distribution of gas medium near and inside the Mach cone. Although radiography has long been used to study the shocks in laser/solid interactions (Hoarty *et al.*, 1997), to the best of our knowledge this is first time that X-radiography has been applied to directly image and quantify the thermodynamic parameters of shock waves generated by liquid jets in a gaseous medium. A schematic showing the data-collection method is illustrated in Fig. 5(*a*), and the model-dependent data fitting is highlighted in Fig. 5(*b*), along with the best fitting models (Fig. 5*c*). In Fig. 5(*b*), absorption curves were generated from the two-dimensional image shown in the last panel (192 μs) of Fig. 4 in a direction normal to the fuel jet direction and at positions of 10.4 mm (circles) and 19.4 mm (squares) behind the spray tip which traveled to 60 mm from the nozzle. The peak in each of the curves at 0 mm is due to absorption in the fuel jet, whereas the peaks near 4 mm (circles) and 9 mm (squares) are from the Mach cone. The solid curves are numeric fits to axially symmetric gas density models. This numerical model is an asymmetric Gaussian distribution across the Mach cone with nearly uniform densities inside and outside the shell of the cone. All image data include about 2 mm spatial smearing due to the 5.13 μs time resolution of the image and to the possible multiple shock fronts near the spray tip (see Fig. 3).

In the plane perpendicular to the jet axis, the shocked region is a cone with an excess density in the SF_6 of ~0.6 μg mm^{-3} measured at 10.4 mm from the jet tip. Behind the high-density region, the interior of the cone has a small but observable reduction in the gas density from the ambient, which implies that decompression has occurred away from the Mach cone. This behavior is different to the compression shock waves generated by a rigid object (Thompson, 1971). Although an independent measurement of the pressure and temperature near the Mach cone is needed to completely characterize the shock waves, the mass distribution of gas near the shock front has never been measured by any other means.

3.2. Results: GDI spray

By using the PAD and the spatially extended X-ray beam at the CHESS D-1 station, synchrotron-radiation-based monochromatic X-radiography was used to image the sprays (Fig. 6*a*). Fig. 6(*b*) shows a sequence of radiographic images, taken at different time instances during the injection. The imaged area shown in each panel is 25 mm (H) × 37 mm (V) with data corrected for the divergence of the X-ray beam. Because the X-ray beam size in the experiment was 13.5 mm (H) × 2.5 mm (V), the imaged area was built up by shifting the position of the injector relative to the beam and the detector, and repeating the injection cycle. Again, the boundaries between these areas can be seen upon close inspection. The exposure time per frame was set to 5.13 μs with subsequent images taken after an additional 15.38 μs delay. Each position shown is the average of images from 20 fuel injection cycles. The measured transmission images were then reduced to projected fuel mass in the X-ray beam according to equation (2). The images (and, even more dramatically, the radiographic animation) show striking details in the dynamic characteristics of the mass distribution of the hollow-cone gasoline spray within 25 mm from the nozzle. These include unexpected time-dependent irregular density distributions and high-frequency density waves within the sprays, features

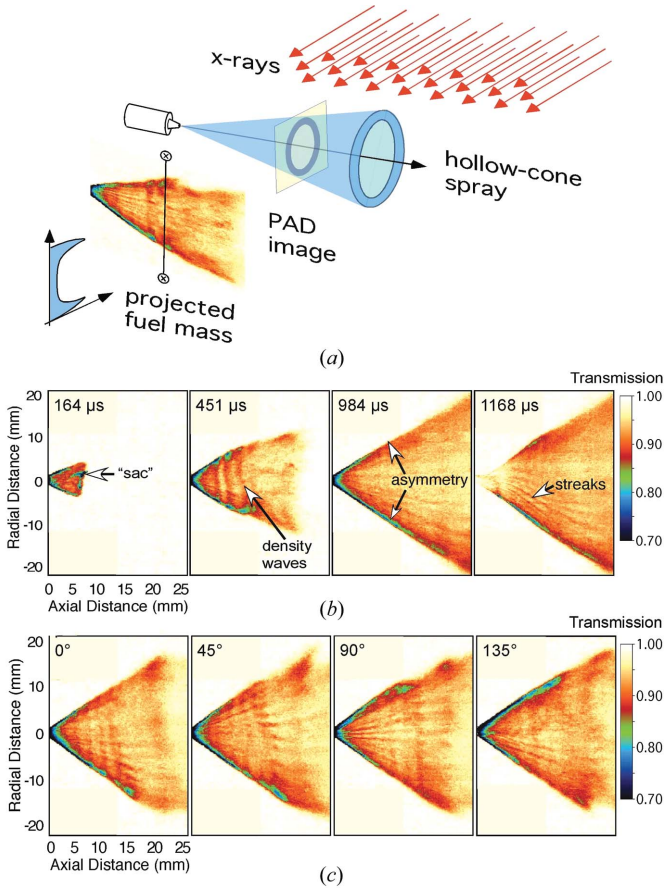

Figure 6
X-radiography of hollow-cone direct-injection fuel sprays: (*a*) schematic of the experiment, (*b*) snapshots of projected fuel mass at various instances, and (*c*) projected fuel mass snapshots taken from four different projection orientations, 0°, 45°, 90°, 135°.

that have never been reported by conventional fuel-spray diagnostic techniques. Additional detailed features, such as axial asymmetry and streaks, are readily evident in these snapshots. More specifically, in Fig. 6(*b*), the snapshots were taken at the instances of 164 μs, when the spray is just exiting the nozzle; 451 μs, when the spray starts to form a stable hollow-cone; 984 μs, when the spray is extended to its full range; and 1168 μs, immediately after the nozzle is closed. Detail features can be found in the fuel distribution, such as a 'sac' (small volume of fuel next to the spray leading edge owing to transient pressure inequilibration at the instance of the injection pintle lift), density waves (owing to instability in pintle axial motion), heavy asymmetry (owing to pintle asymmetric radial motion) and local streaks (owing to nozzle surface finish). Although the axial asymmetry in the spray seemed to have moderated as the spray continued, quantitative analysis revealed that the irregularity still existed throughout the duration of the spray. All these features were amazingly reproducible under identical injection conditions.

It was obvious that such complex spray characteristics could not be analyzed by using a single set of images taken from just one orientation and that images from several spray orientations were needed for a quantitative temporal and spatial analysis of the fuel mass distribution. Tomographic type X-radiographs, as shown in Fig. 6(*c*), were collected from four rotational angles about the spray axis (0°, 45°, 90° and 135° taken at 1107 μs after the start of injection) to facilitate the deconvolution analysis. It was difficult to apply conventional computed tomographic analysis (Romans, 1995; Stock, 1999) and density deconvolution and reconstruction methods (Hammond, 1981; Dasch, 1992) to the spatially complex and transient sprays viewed from only four orientations; therefore, a model-dependent method was developed to reconstruct the time-resolved fuel distribution as follows.

Given the fact that the fuel density distribution was not homogeneous along both angular and radial directions, two layers of iterative fitting models were used. First, an asymmetric cone was constructed based on the obvious irregular deviations from symmetry around the spray axis and by taking advantage of the multiple images taken at various rotational orientations. Second, details of local structure, in the form of several density peaks, were then added to constitute a more complete model. More specifically, the cross section of a hollow-cone spray is a roughly circular-shaped structure, referred to here as a 'cross-sectional ring'. The fuel density can vary along the ring's radial (r) and angular or azimuthal (θ) directions. For the density distribution along the radial direction, the width of the mass density was observed to be different on the inside and outside of maxima at radius $r_0(\theta)$, as $\sigma_1(\theta)$ and $\sigma_2(\theta)$ (Gaussian width), respectively. Taking the peak density, $\rho_0(\theta)$, at radius $r_0(\theta)$ to vary with θ as well, the form for the fuel density becomes

$$\rho(r,\theta) = \rho_0(\theta)\exp\left\{-\left[r - r_0(\theta)\right]^2/2\left[\sigma_k(\theta)\right]^2\right\},$$

where $k = 1$ for $r < r_0$ and $k = 2$ for $r > r_0$. With the limited number of radiographic projections taken, $\rho_0(\theta)$, $r_0(\theta)$ and $\sigma_k(\theta)$ can only be evaluated precisely at the angles corresponding to the regions near the edge portion of each projection, namely, in the vicinity of $\theta_{0i} = n\pi/4$ with $n = 0$ to 7 for the four projections taken in this study. The values of $\rho_0(\theta)$, $r_0(\theta)$ and $\sigma_k(\theta)$ at other angular locations were interpolated with sinusoidal functions, smoothly connecting these points. For example,

$$\rho_0(\theta) = \rho_0[(n+1)\pi/4] + \big(\{\rho_0(n\pi/4) - \rho_0[(n+1)\pi/4]\} \times [1 + \cos(4\theta)]/2\big), \quad (4)$$

in the angular range from $n\pi/4$ to $(n+1)\pi/4$. After the 'global' distribution is modeled, more detailed structures, such as the streaks, were simulated with Gaussian peaks at various angular locations and added to the 'global' distribution. The fuel density in the streaks, based on an N-peak model ($N = 7$), was expressed as

$$\rho_s(r,\theta) = \sum_{i=1}^{N} \rho_{si}^{o} \exp\left[-(\theta - \theta_{ci})^2/2\sigma_{\theta i}^2\right] \times \exp\left\{-\left[r - r_0(\theta)\right]^2/2\sigma_{ri}^2\right\}, \quad (5)$$

where ρ_{si}^{o} is the individual peak density, and θ_{ci}, $\sigma_{\theta i}$ and σ_{ri} are the peak center location and width in the angular and radial

directions, respectively. In a mixed representation using both Cartesian (x, y) and polar (r, θ) coordinates with $r = (x^2 + y^2)^{1/2}$ and $\theta = \tan^{-1}(y/x)$, we assume that the X-ray beam passes through the spray along the x direction and that the y axis is perpendicular to both x and the spray axis. Therefore, the line-of-sight integrated mass profile or instantaneous mass in the beam, $M(y)$, is evaluated by

$$M(y) = A \int \left[\rho(x, y) + \rho_s(x, y)\right] \mathrm{d}x, \qquad (6)$$

where A is the pixel area of the PAD. The mass integration is limited to three standard deviations from $r_0(\theta)$ on either side. The mass deconvolution used a χ^2 regression for curve fitting the experimentally measured data resulting in a best parameter set of $r_0(\theta)$, $\sigma_k(\theta)$ and $\rho_0(\theta)$, as well as other parameters representing local density peaks. These parameters were initially fitted to the four transmission curves independently. To remove the degeneracy of the peaks introduced by the line-of-sight measurement in the cross-sectional ring, the model was consolidated so that it would fit all four data sets simultaneously. Since the deconvolution method was based on models, the self-consistency was verified, since the most realistic single model of fuel distribution fit data from all four imaging directions and the model agreed well with the integrated amount of fuel in the cross section of interest obtained from the radiographic measurements.

With the same reconstruction method, Fig. 7 displays the fitted results or reconstruction from the deconvolution regression to the X-ray transmission data collected from all four rotational angles at 8 mm from the nozzle exit and at 820 µs after the injection, when the hollow-cone spray is fully developed. It is apparent that the fuel density and the cone wall width vary around the ring. The greatest difference in density can be a factor of ten. The variations in the radius of the ring indicate that the cross section of the spray cone is not perfectly circular. The azimuthal dependence of the diameter of the cross-sectional rings and the limited number (four) of mass projection causes the polygonal appearance shown in the calculated rings. Such reconstruction artifacts will diminish as the number of projections increases. Similarly, differences up to 0.8 mm occurred in the cone-wall width showing the strong angular dependence of these parameters. Also present in these fittings are clear localized peaks with which the reliability of the four deconvolution fits can be verified. The projected width and height of these local peaks as shown in Fig. 7 depend on the orientation with which they are viewed.

Fig. 8 shows the cross-sectional density distribution reconstructed from the calculated matrix at four distances, l = 5, 8, 12 and 18 mm, from the nozzle, at 820 µs after the start of injection. The radii of the rings increase away from the nozzle, corresponding to a well developed hollow cone even 5 mm

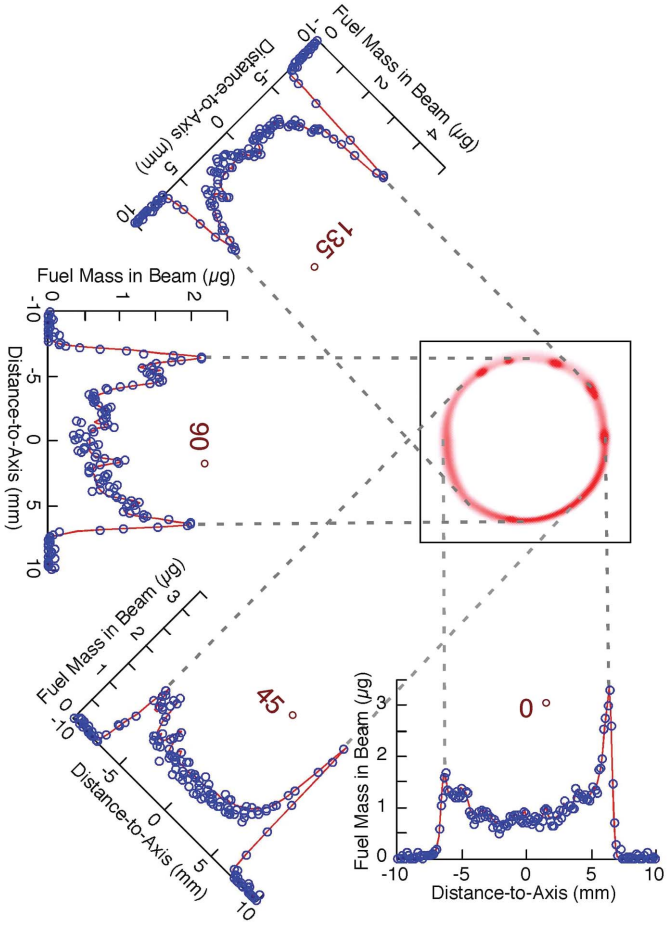

Figure 7
Computed fuel mass distribution by fitting the experimental data (circles) with mass reconstruction models (lines) at time 820 µs and 8 mm from the nozzle at four projection orientations: 0°, 45°, 90° and 135°. A single model, shown as the cross-sectional ring, is used to fit all four sets of the transmission data.

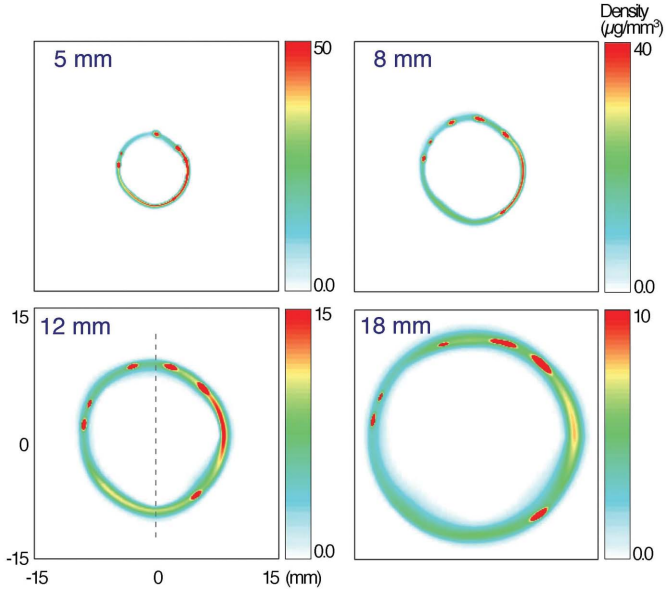

Figure 8
Reconstructed fuel density distribution rings at 820 µs with cross-sectioned slices at 5 mm, 8 mm, 12 mm and 18 mm from the nozzle. The maximum fuel density in any of these cross sections is 105 µg mm^{-3} which is considerably less than the liquid density of the test fuel blend of 840 µg mm^{-3}. The asymmetry of the spray is apparent in the cross-sectional rings and is evaluated quantitatively and summarized in Table 2. The vertical mark (dashed line in the 12 mm cross section) illustrates the halves where the fuel mass values are evaluated.

from the nozzle. This observation clarifies confusion about the hollow-cone development based on measurements using visible-light techniques, where light scattering near the nozzle precluded inference of an unambiguous conclusion. The averaged diameter ($\bar{r}$) of the hollow cone at each location reveals the true cone angle (full) to be 66.2° at this time instance. The average fuel density is greatest near the cone and falls as the spray progresses outwards. However, the maximum density of 105 μg mm^{-3} at only 5 mm from the nozzle is much lower than the liquid density of the test fuel blend (840 μg mm^{-3}), indicating that the fuel had already undergone atomization. A similar result was found for diesel fuel sprays (Powell *et al.*, 2000; MacPhee *et al.*, 2002) but under much higher injection pressures (typically >50 MPa). The physical existence of the localized density peaks is further substantiated by their constant angular positions in rings at different distances from the nozzle. Parameters from the fitting procedure, including the peak fuel density, ρ_0, show a diverse irregularity and are summarized in Table 2, where the spray wall thickness, d, is defined by $(\sigma_1 + \sigma_2)$ (where σ_1 and σ_2 are the values of the outer and inner Gaussian half-width, respectively, as defined previously), and the asymmetry, A_M, of the distribution is defined as $|M_1 - M_2|/(M_1 + M_2)$. Here, M_1 and M_2 are the integrated mass values on each side of the ring separated by the dashed line in Fig. 8 (lower-left panel).

A time series of the cross-sectional fuel density at 12 mm from the nozzle is presented in Fig. 9 at 349 μs, when the spray front just passed the 12 mm mark; 820 μs, when the stable hollow cone formed; 1148 μs, when the nozzle was closed; and 1271 μs, when the trailing edge of the spray was to arrive at the 12 mm mark. Not only does this show the time development of the hollow-cone average diameter, the complexity of the spray dynamics is readily apparent and the asymmetry of the spray persists over the entire injection period. Although the local fuel-density distribution varies rapidly, the overall asymmetry shows that a large fraction of the total amount of fuel was delivered to a limited solid angle. In addition, the features on the rings are relatively stable, with concentrated fuel always on one part of the ring and the local peaks on the other side of the ring. For example, the amounts of fuel during the injection delivered to the halves separated by the dashed mark in Fig. 9 differ by 55%. This observation indicates that the pintle opened asymmetrically throughout the entire injection process. This asymmetry is more clearly shown in an animation of time evolution of the deconvoluted fuel cross-sectional distribution at 15 mm from the nozzle (data not shown).

Table 2
Parameters associated with the fuel distribution at various cross sections of the fuel spray at 820 μs.

The spray wall thickness is defined by $\sigma_1 + \sigma_2$. The asymmetry of the distribution is defined as $|M_1 - M_2|/(M_1 + M_2)$, where M_1 and M_2 are the integrated mass values on each side of the ring separated by the dashed line in Fig. 8.

Distance to nozzle (mm)	Average radius (mm)	Maximum fuel density (μg mm^{-3})	Minimum fuel density (μg mm^{-3})	Maximum wall thickness (mm)	Minimum wall thickness (mm)	Fuel mass asymmetry (%)
5	4.45	1.97	0.22	0.45	0.28	11
8	6.45	1.05	0.19	0.70	0.32	13
12	9.13	1.40	0.12	1.28	0.80	17
18	12.92	1.30	0.09	2.00	1.25	22

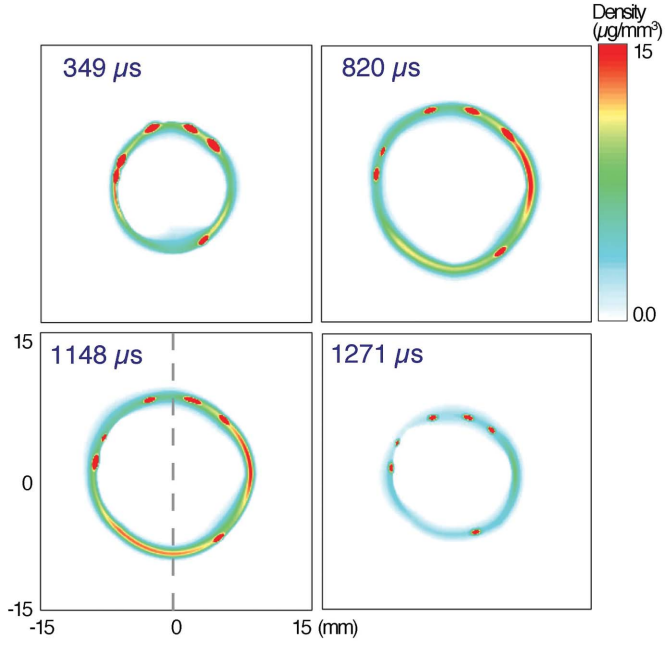

Figure 9
Reconstructed fuel density distribution 12 mm from the nozzle at time instances of 349 μs, when the spray front just passed the 12 mm mark; 820 μs, when the stable hollow-cone formed; 1148 μs, when the nozzle was closed; and 1271 μs, when the trailing edge of the spray was to arrive at the 12 mm mark.

4. Discussion and summary

We have demonstrated that high-pressure fuel sprays can be supersonic and that the Mach cone generated by the supersonic sprays in a gaseous medium can be directly imaged and quantitatively analyzed by X-radiography. Although the manner in which the shock waves affect the atomization of the fuel and the combustion processes are currently unknown, the results will likely draw the attention of spray and combustion researchers to investigate this interesting phenomenon both experimentally and theoretically. With more injection systems adopting preinjection technology (one or a series of short pilot injections before the main injection), the engine cylinders are likely to be filled with a fuel-vapor–air mixture under high temperature before the main spray arrives. It has been recognized that the mixture would have a sonic speed lower than that of either fuel vapor (130 m s^{-1} at room temperature) or air, so the generation of shock waves by the main fuel injection should not be surprising, even at elevated engine-operating temperatures. In this regard, the presence of the dense fill gas used in our study (SF_6) mimics this injection condition.

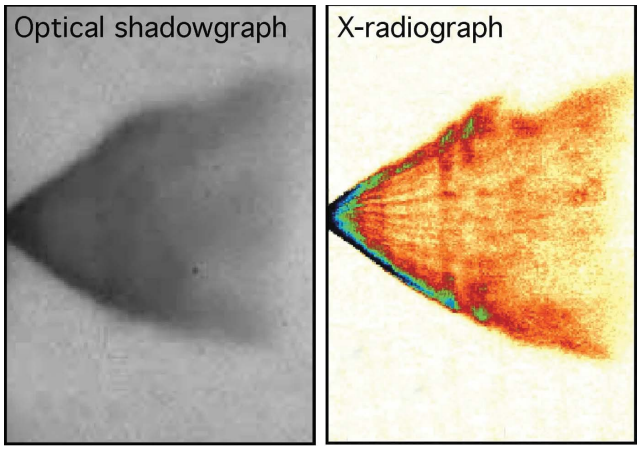

Figure 10
Comparison between images of hollow-cone direct-injection gasoline sprays taken by visible-light shadowgraphy and X-radiography, at the same time instance and under the same injection conditions. Owing to serious multiple scattering by the spray near the nozzle, quantitative evaluation of the fuel density in this region has been difficult with the optical imaging technique. By contrast, the X-ray image directly relates the absorption data to the fuel mass in the X-ray beam. Both the shadowgraph and the X-radiograph are averages of 20 shots.

In the case of the GDI sprays, the severe asymmetry of the fuel distribution may result in uneven combustion and high particulate matter and NO_x emissions since uniform air/fuel mixing cannot be achieved in the chamber. Spray symmetry is considered a key requirement for GDI engines to reduce fuel droplet size in order to increase fuel dispersion and to facilitate full atomization of the fuel before ignition (Zhao *et al.*, 1999). Our results clearly show that both the structure and the dynamics of hollow-cone fuel sprays from nominally symmetric fuel-injector orifices can still be extremely asymmetric, resulting in uneven fuel distribution. The time-resolved quantitative three-dimensional information on the asymmetry and many abnormalities of the sprays revealed in this work, which we have found common to current-generation injectors, may help to explain deficiencies in combustion.

There has been relatively slow progress in understanding fundamental processes in the so-called two-phase or multi-phase fluid dynamics of the high-speed jets that are critical to every fuel injector. In the absence of such understanding, simultaneous optimization of the many variables associated with fuel injectors (*e.g.* the nozzle geometry, fuel pressure, injection chamber gas pressure *etc.*) has been a highly empirical process that effectively has amounted to educated wandering in a complex multidimensional space. Part of the reason for the lack of progress has been the dearth of experimental methods to validate computational fluid dynamics modeling efforts. The X-radiographic method described here may well provide the needed information. Currently, the 5 μs time resolution is a combination of the image integration time and jitter associated with the coordination of the start of the image integration with the start of the injection cycle with the timing jitter less than 300 ns. Improved time resolution would be possible if, instead of the bending-magnet beamlines used in this study, beamlines with higher intensity, such as insertion-device beamlines at either the APS or CHESS, were used. With these higher fluxes, the PAD, capable of submicrosecond imaging, could image the spray at higher speeds with single shots if required.

We conclude that rapid-framing nonintrusive monochromatic X-ray radiography and tomography are well suited to characterization of the critical difficult-to-measure parts of the fuel-injection process that are required to optimize engine combustion performance. As shown in Fig. 10, compared with conventional optical methods, this technique provides the transient spatial distribution of fuel mass, whether in liquid or vapor form, which has been otherwise difficult to measure, in this optically dense near-nozzle region. We also believe that a more comprehensive understanding of the factors affecting the fuel-density distribution over time will enable the development of more realistic and complex computer models of the spray. This is important since experimentation with an actual engine is a lengthy and costly process. The methodology demonstrated here is obviously also suitable to study the fluid dynamics of other high-speed liquid sprays in situations that do not readily lend themselves to analysis by optical methods, such as in spray coaters, ink-jet apparatus, dense plasmas and mixing chambers.

The author acknowledges that the results are from the collaborative research with Christopher F. Powell, Wenyi Cai, Yong Yue, Andrew MacPhee and Suresh Narayanan of Argonne National Laboratory (ANL), Sol Gruner, Mark Tates, Matthew Renzi, Alper Ercan and Ernest Fonte of Cornell University, Johannes Schaller and Jochen Walter of Robert Bosch GmbH. The author is thankful to Ramesh Poola for his initiation and participation of the research. Technical support from Armon. L. McPherson, Jinyuan Liu, Roy Cuenca (ANL), Joerg Fettes, Kevin Berta, Phillip Bohl and Manfred Schlebusch (Robert Bosch Corporation, USA), Donald Moran, Gail E. Geiger and Paul G. VanBrocklin (Delphi Corporation) is greatly appreciated. This work is supported by the ANL grants, FreedomCAR and Vehicle Technology Program of the US Department of Energy (DOE). The use of the APS is supported by the US DOE under contract W-31-109-ENG-38. We gratefully acknowledge staff support at 1-BM beamline of the APS, and at D1 beamline of CHESS which is funded by the US National Science Foundation (NSF) and the US National Institute of General Medical Sciences *via* NSF under award DMR-9713424. PAD detector development was funded by DOE grants DE-FG-0297ER14805 and DE-FG-0297ER62443 to Sol Gruner.

References

Adrian, R. J. (1991). *Annu. Rev. Fluid Mech.* **23**, 261–304.
Barna, S. L., Shepherd, J. A., Tate, M. W., Wixted, R. L., Eikenberry, E. F. & Gruner, S. M. (1997). *IEEE Trans. Nucl. Sci.* **44**, 950–956.
Beeck, M. A. & Hentschel, W. (2000). *Opt. Lasers Eng.* **34**, 101–120.
Cai, W., Powell, C. F., Yue, Y., Narayanan, S., Wang, J., Tate, M. W., Renzi, M. J., Ercan, A., Fontes, E. & Gruner, S. M. (2003). *Appl. Phys. Lett.* **83**, 1671–1673.

Cao, Z.-M., Nishino, K., Mizuno, S. & Torii, K. (2000). *JSME Int. J. Ser. B*, **43**, 582–589.
Char, J. M., Kuo, K. K. & Hsieh, K. C. (1990). *J. Propuls.* **6**, 544–551.
Chigier, N. (1991). *Prog. Energy Combust. Sci.* **17**, 211–262.
Council, N. R. (2001). *Effectiveness and Impact of Corporate Average Fuel Economy (CAFE) Standards.* Washington, DC: National Academy Press.
Dasch, C. J. (1992). *Appl. Opt.* **31**, 1146–1152.
Field, J. E. & Lesser, M. B. (1977). *Proc. R. Soc. London A*, **357**, 143–162.
Fujikawa, T., Hattori, Y., Koike, M., Akihama, K., Kobayashi, T. & Matsushita, S. (1999). *JSME Int. J. Ser. B*, **42**, 760–767.
Hammond, J. D. C. (1981). *Appl. Opt.* **20**, 493–499.
Hecht, E. (1998). *Optics.* Reading, MA: Addison-Wesley.
Henke, B. L., Gullikson, E. M. & Davis, J. C. (1993). *Atom. Data Nucl. Data Tables*, **54**, 181–342.
Hentschel, W. & Schindler, K.-P. (1996). *Opt. Lasers Eng.* **25**, 401–413.
Herman, H. (1988). *MRS Bull.* **13**, 60–67.
Hoarty, D., Iwase, A., Meyer, C., Edwards, J. & Willi, O. (1997). *Phys. Rev. Lett.* **78**, 3322–3325.
Hoffman, J., Martin, J. K. & Coates, S. W. (1997). *Rev. Sci. Instrum.* **68**, 4247–4252.
Hurly, J. J., Defibaugh, D. R. & Moldover, M. R. (2000). *Int. J. Thermophys.* **21**, 739–765.
Kuo, K. (1996). Editor. *Recent Advances in Spray Combustion: Spray Atomization and Drop Burning Phenomena. Progress in Astronautics.* Reston, VA: American Institute of Aeronautics and Astronautics.
Lang, J. C., Srajer, G., Wang, J. & Lee, P. L. (1999). *Rev. Sci. Instrum.* **70**, 4457–4462.
Lee, C. S., Lee, K. H., Chon, M. S. & Kim, D. S. (2001). *At. Sprays*, **11**, 35–48.
MacPhee, A., Tate, M. W., Powell, C. F., Yue, Y., Renzi, M. J., Ercan, A., Narayanan, S., Fontes, E., Walter, J., Schaller, J., Gruner, S. M. & Wang, J. (2002). *Science*, **295**, 1261–1263.
O'Keefe, J. D., Wrinkle, W. W. & Scully, C. N. (1967). *Nature (London)*, **213**, 23–25.
Parrish, S. & Farrell, P. V. (1997). *Transient Spray Characteristics of a Direct-Injection Spark-Ignited Fuel Injector.* SAE Paper 970629. Warrendale, PA: Society of Automotive Engineers.
Powell, C. F., Yue, Y., Poola, R. & Wang, J. (2000). *J. Synchrotron Rad.* **7**, 356–360.
Romans, L. E. (1995). *Introduction to Computed Tomography.* Baltimore: William and Wilkins.
Rossi, G., Renzi, M. J., Eikenberry, E. F., Tate, M. W., Bilderback, D., Fontes, E., Wixted, R., Barna, S. & Gruner, S. M. (1999). *J. Synchrotron Rad.* **6**, 1096–1105.
Sick, V. & Stojkovic, B. (2001). *Appl. Opt.* **40**, 2435–2442.
Spearot, J. A. (2001). *Advanced Engine and Fuel Systems Development for Minimizing Carbon Dioxide Generation, Carbon Management: Implications for R&D in the Chemical Sciences and Technology. A Workshop Report to the Chemical Sciences Roundtable.* Washington, DC: National Academy Press.
Stock, S. R. (1999). *Int. Mater. Rev.* **44**, 141–164.
Summers, D. A. (1995). *Waterjetting Technology.* London: Spon.
Thompson, P. A. (1971). *Compressible-Fluid Dynamics.* New York: McGraw-Hill.
Tikhomirov, R. A., Babanin, V. F., Petukhov, E. N., Starikov, I. D. & Kovalev, V. A. (1992). *High-Pressure Jetcutting.* New York: ASME Press.
Ullom, M. J. & Sojka, P. E. (2001). *Rev. Sci. Instrum.* **72**, 2472–2477.
Woodward, R. D., Pal, S. Santoro, R. J. & Kuo, K. K. (1995). *Recent Advances in Spray Combustion: Spray Atomization and Drop Burning Phenomena*, pp. 185–210. Reston, VA: American Institute of Aeronautics and Astronautics.
Yule, A. J. & Watkins, A. P. (1990). *At. Sprays*, **1**, 199–204.
Zhang, Y.-Y., Yoshizaki, T. & Nishida, K. (2000). *Appl. Opt.* **39**, 6221–6229.
Zhao, F., Lai, M.-C. & Harrington, D. L. (1999). *Prog. Energy Combust. Sci.* **25**, 437–562.